

See discussions, stats, and author profiles for this publication at: <https://www.researchgate.net/publication/228486096>

Pt–Co Bimetallic Catalyst Supported on Single-Walled Carbon Nanotubes: Effect of Alloy Formation and Oxygen Containing Group†

ARTICLE in THE JOURNAL OF PHYSICAL CHEMISTRY C · MAY 2010

Impact Factor: 4.77 · DOI: 10.1021/jp102511k

CITATIONS

24

READS

13

4 AUTHORS, INCLUDING:



Xiaoming Wang

BASF SE

19 PUBLICATIONS 328 CITATIONS

SEE PROFILE

Pt–Co Bimetallic Catalyst Supported on Single-Walled Carbon Nanotubes: Effect of Alloy Formation and Oxygen Containing Groups[†]

Xiaoming Wang, Nan Li, Lisa D. Pfefferle, and Gary L. Haller*

Department of Chemical Engineering, Yale University, New Haven, Connecticut 06520

Received: March 19, 2010; Revised Manuscript Received: May 14, 2010

Pt monometallic and Pt–Co bimetallic catalysts have been prepared on single-walled carbon nanotubes (SWNT) with and without HNO₃ treatment. The HNO₃ treatment introduced oxygen containing groups (OCGs), which affect both the structure and activity of the catalyst. The introduction of OCGs does not affect the structure of Pt monometallic catalysts but increased the dispersion in the bimetallic catalysts. The aqueous phase re-forming (APR) activity of the bimetallic catalysts is also affected by the OCGs, because the local concentration of the reactant around the SWNT support with OCGs is less than the case without OCGs. The two effects act on activity in opposing directions so the bimetallic catalysts on the two supports give similar APR yields, but this discovery gives us direction and a basis for the future design and improvement of SWNT supported catalysts.

1. Introduction

The hydrogen fuel cell is of growing interest as an electrical power source.^{1–3} Although the fuel cell itself is environmentally benign, the traditional production of hydrogen has been via high temperature steam re-forming of nonrenewable hydrocarbon feedstocks.^{4,5} Aqueous phase reforming (APR), as recently developed by Dumesic and co-workers,^{6–11} offers a new route to produce hydrogen from oxygenated hydrocarbons (which can be obtained from biomass), at mild temperature and modest pressure above atmospheric. This process also offers low CO content in the product, which is highly desirable for fuel cell applications.^{1,3,12}

APR has been carried out on different metals¹⁰ and different supports.⁷ While most oxide supports gradually dissolve in water at the reaction conditions of APR, we have been using carbon nanotubes (CNT) as the support for APR catalysts^{13,14} to maintain the catalyst stability in an aqueous environment at elevated temperatures and pressures. Both single-walled carbon nanotubes (SWNT)¹⁴ and multiwalled carbon nanotubes (MWNT)¹³ have been used as catalyst supports for Pt used for APR. To help improve the dispersion of the Pt catalysts, CNT are often treated with HNO₃ to create oxygen containing groups (OCGs) on the CNT surface.^{13,15,16} However, we have found that, although the introduction of OCGs increased the catalyst dispersion on MWNT, for some reactions the turnover frequency (TOF) can decrease so that the total conversion also decreased. This observation appears to be true only for reactions with a binary mixture of reactants and is attributed to the competitive adsorption of the two components on the catalyst surface.¹³ As the introduction of OCGs increases the hydrophilicity of the CNT support, it tends to preferentially adsorb hydrophilic reactants, thus changing the ratio, and perhaps the total local concentration, of reactants around the Pt particles on the CNT supports. The OCGs on the MWNT can be removed by high temperature annealing under an inert atmosphere, and the activity of the catalyst is recovered after the removal of OCGs.

This treatment does not affect the dispersion of Pt, presumably because of Pt anchoring to defects that are retained after high temperature annealing.

Our previous work also suggested that OCGs have a more profound negative affect on the catalytic activity of SWNT supported catalysts compared with MWNT supported catalysts,¹⁴ because for SWNT supported catalysts, the majority of the Pt particles are located outside the nanotubes, due to the small inner cavity of the SWNT, while for MWNT supported catalysts, a large portion of the particles can be inside the tubes, where the OCGs are absent, or at least of a much lower concentration.

We have also discovered that by introducing a Co component, the Pt–Co bimetallic catalyst has higher activity than the Pt monometallic catalyst when supported on HNO₃-treated SWNT.¹⁴ In this report, a detailed study has been carried out on Pt monometallic and Pt–Co bimetallic catalysts supported on both as-received and HNO₃-treated SWNT, and the effects of the bimetallic alloy phase formation and of OCGs with the bimetallic catalysts are discussed.

2. Experimental Section

2.1. Catalyst Preparation. The SWNT were purchased from Cheap Tubes Inc., with a specific surface area of 407 m²/g and pore volume of 2.0 cm³/g, characterized by nitrogen physisorption at 77 K. To create OCGs, the SWNT were refluxed in 2.6 M HNO₃ (diluted from 69 wt % concentrated HNO₃ from J. T. Baker) overnight, filtered, washed with ethanol, and dried at 70 °C. The as-received and HNO₃-treated commercially provided SWNT are denoted as cSWNT-r and cSWNT-n, respectively.

The Pt monometallic catalysts were prepared by incipient wetness impregnation, and the Pt–Co bimetallic catalysts were prepared by sequential impregnation, following the procedure in our previous paper.¹⁴ The Pt loading in the monometallic catalysts is 8.0 wt % (2.5 at. %) for both Pt/cSWNT-r and Pt/cSWNT-n, which is confirmed by the edge jump of the X-ray absorption spectra,¹⁷ and the Pt–Co bimetallic catalysts, Pt–Co/cSWNT-r and Pt–Co/cSWNT-n, are prepared by impregnation of a Co precursor solution on the monometallic catalysts, keeping the 1:1 weight ratio (1:3.31 atomic Pt:Co ratio) between

[†] Part of the “D. Wayne Goodman Festschrift”.

* Corresponding author. Tel: +1 230 432 4378. Fax: +1 203 432 4387. E-mail: gary.haller@yale.edu.

Pt and Co and 8 wt % Pt relative to SWNT as in the monometallic catalyst.

2.2. Catalyst Characterization. **2.2.1. Near Edge X-ray Absorption Fine Structure (NEXAFS).** Both carbon and oxygen K edge NEXAFS spectra of the SWNT supports were taken at beamline U7A, National Synchrotron Light Source (NSLS), Brookhaven National Laboratory (BNL). The sample was pressed into a pellet, which was then adhered onto a sample bar, and inserted into the ultrahigh vacuum chamber for NEXAFS measurement. The partial electron yield (PEY) signal was collected with entrance grid bias voltages at -40 V at the carbon K edge. The PEY at the oxygen K edge was also collected with the same entrance grid bias voltage, and the oxygen content can be calculated from the relative edge jump intensities at the carbon and oxygen K X-ray absorption edges.

2.2.2. Raman Spectroscopy. Raman spectra of cSWNT-r and cSWNT-n powder samples were collected on a JASCO NRS-3100 laser Raman spectrometer with excitation wavelength of 532 nm.

2.2.3. X-ray Absorption Spectroscopy (XAS). The X-ray absorption spectroscopy (XAS), including both X-ray absorption near edge structure (XANES) and extended X-ray absorption fine structure (EXAFS), was carried out at beamline X18B, NSLS, Brookhaven National Laboratory, for both the Pt L_{III} edge and the Co K edge, to investigate the electronic state and coordination environment of the metals in the catalysts, following the procedures of our previous paper.¹⁴ Thirty milligrams of the catalyst was well-mixed with 270 mg of boron nitride powder by grinding, and then the mixture was pressed into a self-standing pellet. The pellet was placed into an in situ reaction cell with two beryllium windows, and then the cell is sealed with a copper gasket to prevent any possible leakage. In-situ hydrogen reduction was carried out at the beamline at 400 °C for 30 min, with time-resolved XANES spectra taken, and EXAFS spectra were taken after the system was cooled to room temperature by liquid nitrogen. A residual gas analyzer (RGA) with mass spectrometer detector is connected to the outlet of the in situ cell. The EXAFS data was analyzed and fitted using the IFEFFIT 1.2.11 software package.^{18,19}

2.2.4. Chemisorption. Both hydrogen and CO chemisorption of the catalysts were carried out on a Quantachrome Autosorb-1-C instrument. Fifty milligrams of each catalyst was placed in a quartz cell, held by two pieces of quartz wool at either end. The catalysts were reduced at 400 °C in hydrogen, and then the cell was evacuated at the same temperature for 2 h. The cell was then cooled to 40 °C, and the adsorbates were introduced. The adsorption isotherms were recorded between 80 and 560 mmHg. After the first isotherm (the total adsorption isotherm) was taken, the cell was subjected to evacuation again to remove the weakly adsorbed adsorbates, and a second adsorption isotherm (the weak adsorption isotherm) was recorded. The irreversible adsorption isotherm was obtained by taking the difference between the total and the weak adsorption isotherms. Two apparent dispersions of the catalysts can be calculated by extrapolating either the total or the irreversible isotherm to zero pressure and assuming one hydrogen atom or CO molecule per surface metal atom.

2.2.5. Infrared (IR) Spectroscopy. One milligram of catalyst, prereduced at 400 °C, was mixed and ground with 120 mg of KBr (IR grade, from Sigma-Aldrich), and the mixture was pressed into a pellet. The pellet was then placed into the measurement chamber of a Nicolet NEXUS 870 FTIR spectrometer. The chamber was purged with nitrogen for 30 min to

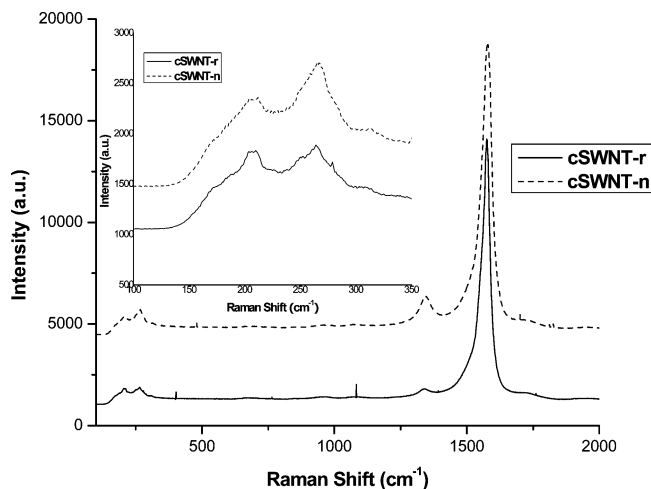


Figure 1. Raman spectra of cSWNT before and after nitric acid treatment.

eliminate noise from atmospheric water and CO_2 , and then the spectrum was taken in the transmission mode.

2.2.6. Transmission Electron Microscopy (TEM). One milligram of prereduced catalyst was sonicated in 10 mL of ethanol for 30 min, and then a drop of the suspension was placed on a TEM grid with a holey carbon film, and dried in air. The TEM images were taken by a Philips Tecnai 12 TEM operated at 120 kV.

2.3. Aqueous Phase Re-forming (APR) Activity Measurement. Activity for the aqueous phase reforming (APR) reaction was measured in a fixed bed reactor described elsewhere.¹⁰ Fifty milligrams of catalyst was placed in a stainless steel reactor, held in place by quartz wool at both ends. The catalysts were prereduced at 400 °C for 30 min, and then the system was purged by nitrogen. The reaction was carried out at 225 °C and 380 psig, and 10 wt % ethylene glycol aqueous solution was fed into the reactor at 60 $\mu\text{L}/\text{min}$ by an HPLC pump. The gaseous products were detected by an online Varian CP-3800 gas chromatography.

3. Results and Discussion

3.1. Nitric Acid Treatment of SWNT. The HNO_3 treatment of SWNT introduced OCGs, as well as defect sites, on the SWNT. The defect sites can be characterized by Raman spectra as shown in Figure 1. There are three characteristic peaks for SWNT Raman spectra:^{20,21} the G band at around 1580 cm^{-1} showing the sp^2 (graphitic) feature, the D band at around 1350 cm^{-1} showing the sp^3 (defect) feature, and the radial breathing mode (RBM) peaks below 400 cm^{-1} , which are dependent on the diameters of the nanotubes. The RBM peaks of cSWNT-r and cSWNT-n are very similar (see the inset of Figure 1), indicating that the HNO_3 treatment has negligible effect on the diameter distribution of the carbon nanotubes. However, the intensity of the D band obviously increased after the HNO_3 treatment, suggesting the formation of new defect sites.^{22,23} The introduction of OCGs can be verified by the oxygen content calculated from the NEXAFS spectra.²⁴ A summary of the changes of SWNT after HNO_3 treatment is listed in Table 1. Some carbon atoms were oxidized into gaseous carbon, causing the weight loss, while the majority is still left in the carbon nanotubes. Compared with cSWNT-r, cSWNT-n has a much higher oxygen content, and the higher defect density (from the ratio between G band and D band areas from Raman spectra), which is due to the oxidation by HNO_3 . The amount of OCGs and the defect density are highly correlated.

TABLE 1: Effect of HNO₃ Treatment

sample	weight loss after HNO ₃ treatment (%)	oxygen content calculated from NEXAFS (%)	G/D ratio from Raman spectra
cSWNT-r	N/A	1.3	62.2
cSWNT-n	8.2	6.2	17.4

TABLE 2: Hydrogen and CO Chemisorption Results^a

catalyst	adsorbate	dispersion		$D_{\text{irr}}/D_{\text{t}}$
		D_{t} (%)	D_{irr} (%)	
Pt/cSWNT-r	H ₂	45.35	19.59	0.43
	CO	31.96	25.90	0.81
Pt/cSWNT-n	H ₂	45.20	16.90	0.37
	CO	31.50	24.38	0.77
Pt–Co/cSWNT-r	H ₂	24.77	5.67	0.23
	CO	38.20	27.00	0.71
Pt–Co/cSWNT-n	H ₂	41.00	7.67	0.19
	CO	60.40	45.67	0.76

^a D_{t} is calculated from the total isotherms. D_{irr} is calculated from the irreversible isotherms. Dispersion is defined as the ratio between the number of H atoms or CO molecules and total number of Pt atoms.

3.2. Aqueous Phase Reforming Activity of the Catalysts.

The hydrogen and CO chemisorption results of the catalysts are summarized in Table 2. The discrepancy between the dispersion calculated from irreversible and total chemisorption isotherms from CO chemisorption is not very large, and the ratio between these two dispersions ($D_{\text{irr}}/D_{\text{t}}$) from CO chemisorption is almost a constant and is consistent with our previous results with MWNT supported catalysts.¹³ However, the discrepancy between irreversible and total dispersion from hydrogen chemisorption is more obvious and can be correlated with the electronic structure of the catalysts, as suggested by previous results from us as well as other groups.^{13,25,26} It has been suggested that the reversible (weak) adsorption is also chemisorptive,²⁵ so the dispersion from the total adsorption isotherm, D_{t} , will be used to calculate the turnover frequency (TOF) of the APR reaction. But whether to use the dispersion from CO or hydrogen chemisorption remains an issue. That higher apparent dispersion measured from hydrogen chemisorption when compared to CO chemisorption on the same catalyst has been attributed to the hydrogen spillover onto the carbon nanotubes,¹³ so it has been suggested that CO chemisorption results should be used in the calculation of TOF for better accuracy, at least for Pt monometallic catalysts. But in the case of Pt–Co bimetallic catalysts, since Co is inactive for hydrogen chemisorption but is active for CO chemisorption, the dispersions from CO chemisorption are higher than that from hydrogen chemisorption for Pt–Co bimetallic catalysts (because the dispersion is based only on Pt). However, whether the Co sites are active for APR is not clear yet. It has been discovered that a Co monometallic catalyst has negligible activity in APR, but Pt–Co bimetallic catalysts have much higher activity than Pt monometallic catalyst, which cannot be simply explained by the bimetallic alloying effect.¹⁰ Similar results have also been reported by Chen et al.^{27–30} for the benzene hydrogenation reaction, when Co monometallic and Pt monometallic catalysts show relatively low activity, Pt–Co bimetallic catalysts, with 1.2 wt % Pt and 10–30 wt % Co, show much higher activity, with apparent activation energy close to the Co monometallic catalyst in this case. Given the close values of the apparent activation energies of Co monometallic and Pt–Co bimetallic catalysts, as well as the large Co:Pt ratio (molar ratio as large as 80), their experimental results lead to the conclusion that Co

could possibly be an active metal for benzene hydrogenation, but only with the existence of Pt due to some synergistic effect between Pt and Co. This conclusion is probably also true for APR.

Table 3 lists the APR activity and selectivity data for the four catalysts discussed in this paper, and TOF values have been calculated using both hydrogen chemisorption results and CO chemisorption results. Coincidentally, for all catalysts except Pt/cSWNT-n, the mass time yields are very similar but become different when normalized by the number of active sites. If hydrogen chemisorption results are used to calculate TOF (i.e., TOF1 in Table 3), meaning for the bimetallic catalysts, only surface Pt atoms are considered as active sites, the Pt–Co bimetallic catalysts on both supports have higher activities than Pt monometallic catalysts on the same support. But this is not the case if we consider both Pt and Co are active, the assumption used if we base the TOF on CO chemisorption. However, in both monometallic and bimetallic catalysts, the cSWNT-r supported catalysts always give higher activity than cSWNT-n supported catalysts, and it is more obvious for Pt monometallic catalyst (in the case of TOF1, 2.15 min^{−1} versus 0) than for Pt–Co bimetallic catalysts (3.76 min^{−1} versus 2.35 min^{−1} for TOF1). The difference, as in catalyst performance on different supports, can be related to a higher concentration of OCGs on cSWNT-n than on cSWNT-r, and will be discussed in detail in section 3.4.

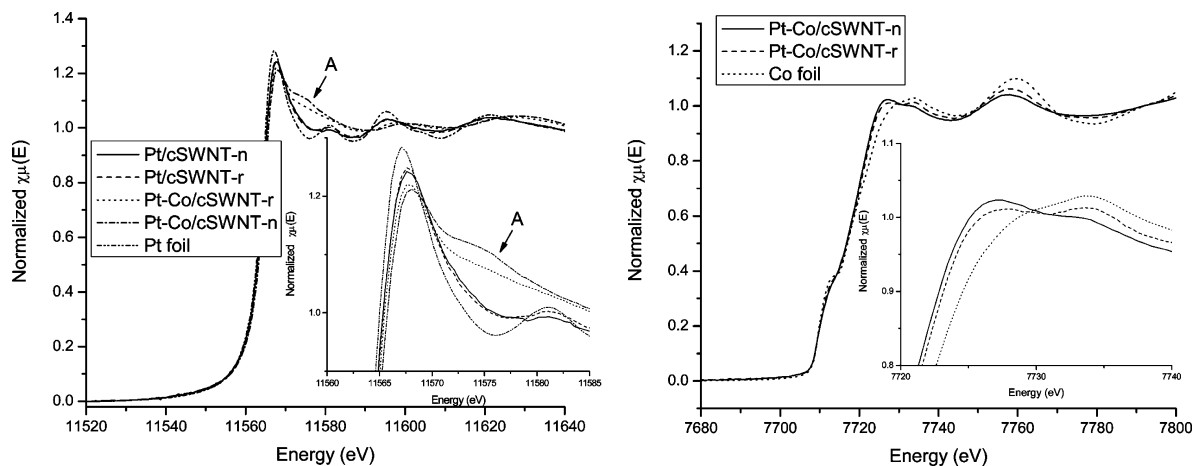
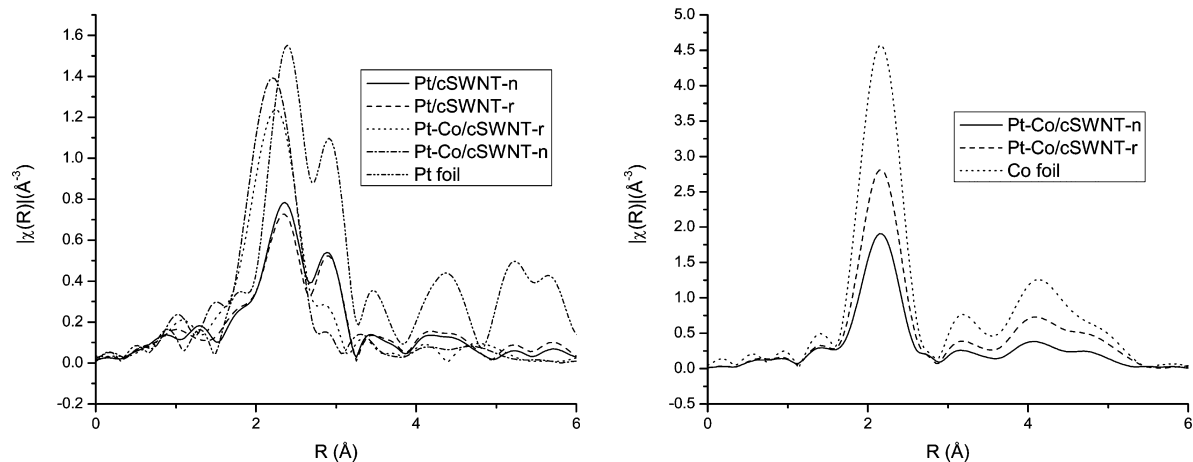
3.3. Structural Analysis. Structural analysis of the catalysts has been carried out by XAS, including both XANES and EXAFS. The XAS results of Pt/cSWNT-n and Pt–Co/cSWNT-n have been published in our previously paper, and here the results will be compared with those for Pt/cSWNT-r and Pt–Co/cSWNT-r.

Both Pt L_{III} edge and Co K edge XANES spectra of the catalysts are shown in Figure 2, in comparison with those for Pt foil and Co foil, respectively. Regarding the white line at the Pt L_{III} edge, at least two physical phenomenon can affect the intensity of the white line: the size of the cluster, which can be considered as an intrinsic effect (density of state of nanometer scale Pt clusters are far from that of the bulk), and a possible charge transfer between the cluster and the support, which can be considered as an extrinsic factor.³¹ All the white lines of the catalysts in the spectra of the Pt L_{III} edge are lower than those of the Pt metal and are shifted to higher binding energy. For monometallic catalysts, this is due to the chemisorbed hydrogen remaining on the surface Pt sites.^{13,14,32,33} For bimetallic catalysts, the white line intensities are even lower, and a new feature, i.e., a shoulder, rises at about 11 575 eV (point A in Figure 2a), which can be attributed to the formation of Pt–Co bonding.^{34,35} In the case of nanometer scale metallic clusters, special attention has to be paid to different structural parameters, for example, the size and morphology of the cluster, the interatomic distance (taking into account contraction/dilatation processes), and the presence of heterometallic bonds (in the case of bimetallic clusters) to analyze the K edge of 3d metals.³⁶ The XANES spectra at the Co K edge of the two bimetallic catalysts show very little difference. The Pt–Co/cSWNT-n has a slightly higher white line intensity than Pt–Co/cSWNT-r at the Co K edge, and both are much higher than the that of Co foil. For both bimetallic catalysts, the Pt L_{III} edge XANES spectra show lower white line intensity than the Pt foil and the Pt monometallic catalysts, and the Co K edge XANES spectra show higher white line intensity than the Co foil. These results indicate that for the two bimetallic catalysts, the Pt atoms in the catalysts have lower electron densities at the Fermi level

TABLE 3: Aqueous Phase Re-forming Activities of Different Catalysts

catalyst	catalyst mass time yield ^a	Pt mass time yield ^b	hydrogen selectivity ^c	alkane selectivity ^d	TOF1 (min ⁻¹) ^e	TOF2 (min ⁻¹) ^f
Pt/cSWNT-r	1.74 ^h	25.0 ^h	81.8% ^h	8.9% ^h	2.15	3.05
Pt/cSWNT-n	N/A ^{g,h}	N/A ^{g,h}	N/A ^{g,h}	11.7% ^h	N/A ^g	N/A ^g
Pt-Co/cSWNT-r	1.72	23.9	93.3%	5.2%	3.76	2.44
Pt-Co/cSWNT-n	1.78	24.7	~100%	7.1%	2.35	1.59

^a Measured by millimole hydrogen per gram of catalyst per minute. ^b Measured by millimole hydrogen per gram of platinum in the catalyst per minute. ^c Calculated as (molecules of H₂ produced/C atoms in gas phase)/(2/5). ^d Calculated as (C atoms in gaseous alkanes)/(total C atoms in gas phase product). ^e Calculated as the number of ethylene glycol molecules consumed per active Pt site (measured by hydrogen chemisorption) within unit time. ^f Calculated as the number of ethylene glycol molecules consumed per active Pt site (measured by CO chemisorption) within unit time. ^g The hydrogen yield of this catalyst is below the detection limit of the gas chromatography. ^h Data from ref 14.

**Figure 2.** XANES results of catalysts at (a) Pt LIII edge and (b) Co K edge.**Figure 3.** R space EXAFS results of catalysts at (a) Pt LIII edge and (b) Co K edge.

than the Pt foil and the Pt monometallic catalysts, while the Co atoms have higher electron densities at the Fermi level than the Co foil, indicating that Pt and Co probably form an alloy phase in these two catalysts, and there should be a charge transfer between Pt and Co, i.e., some electron transfer from Co to Pt.^{34,35,37} Given the electronegativity of Pt and Co, this charge transfer direction is reasonable.

The EXAFS R space spectra, i.e., the k^2 weighed Fourier transform of EXAFS spectra, without phase correction, are shown in Figure 3, in comparison with those for Pt and Co foils, respectively. From the Pt L_{III} edge spectra, both monometallic catalysts contain Pt(0) nanoparticles with very small particle size, as the shape of their spectra is similar to that of Pt foil with much lower intensity. The fitting of the spectra gives the average first shell Pt–Pt coordination number, and the

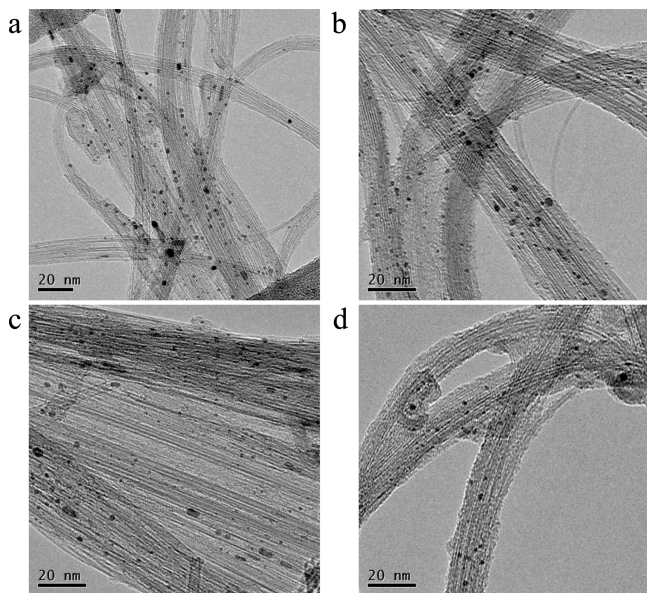
average particle size of the Pt nanoparticles from the average first shell coordination number, using the structure model developed by Calvin et al.,^{38,39} and the results are listed in Table 4. The particle sizes of these two catalysts from EXAFS are very similar, which can be verified also by the very close chemisorption results, as well as the TEM images in Figure 4a,b.

The EXAFS of bimetallic catalysts, on the other hand, gives more information. At the Pt L_{III} edge, the peaks in their EXAFS R space spectra of both Pt–Co/cSWNT-r and Pt–Co/cSWNT-n have a negative shift by about 0.2 Å compared with the spectral peaks of the Pt foil, which is due to the formation of the Pt–Co alloy bonding.^{34,35,37} No peak or shoulder can be observed at the position of Pt–Pt bonding for the bulk Pt foil, indicating that almost all of the Pt atoms in the bimetallic catalysts are in

TABLE 4: EXAFS Fitting Results for Pt Monometallic Catalysts

catalyst	CN ^a	dR (Å) ^b	R (Å) ^c	d _p (nm) ^d
Pt/cSWNT-r	8.26 (1.03) ^d	0.03 (0.01) ^d	2.74 ^e	1.31 ^e
Pt/cSWNT-n	7.80 (0.80) ^{d,f}	0.03 (0.00) ^{d,f}	2.74 ^{e,f}	1.16 ^{e,f}

^a First shell average coordination number of each absorber–scatterer pair. ^b Deviation from the interatomic distance in pure metal, which is 2.77 Å for Pt. ^c Calculated bond length from dR. ^d Data from the first shell coordination number fitting; data in the brackets are uncertainties given by the IFEFFIT software. ^e These data are not directly from the fitting, thus uncertainty data are not included. ^f Data from ref 14.

**Figure 4.** TEM images of (a) Pt/cSWNT-r, (b) Pt/cSWNT-n, (c) Pt–Co/cSWNT-r, and (d) Pt–Co/cSWNT-n.

the alloy phase. The EXAFS R space spectra of Co K edge of the two bimetallic catalysts, on the other hand, both show a main peak at the position of bulk Co–Co bond, with lower intensity, indicating that Co–Co bonding is dominant for Co, and the Co atoms form small Co clusters. Pt–Co/cSWNT-n has much smaller Co clusters than Pt–Co/cSWNT-r, as suggested by the intensity of R space EXAFS spectra.

The first shell coordination number fitting was conducted with data from both the Pt L_{III} edge and the Co K edge concurrently, with the following constraints applied during the fitting:^{40,41}

$$\text{CN}_{\text{Co–Pt}} = \text{CN}_{\text{Pt–Co}} \cdot x_{\text{Pt}}/x_{\text{Co}} \quad (1)$$

$$R_{\text{Pt–Co}} = R_{\text{Co–Pt}} \quad (2)$$

$$\sigma_{\text{Pt–Co}}^2 = \sigma_{\text{Co–Pt}}^2 \quad (3)$$

Here CN_{Co–Pt} is the average coordination numbers of Pt around Co, i.e., the total number of Co–Pt bonds from Co EXAFS normalized to the total number of Co atoms, and CN_{Pt–Co} is the average coordination number of Co around Pt, i.e., the total number of Pt–Co bonds from Pt EXAFS normalized by total number of Pt atoms. x_{Pt} and x_{Co} are the atomic mole fractions, $x_{\text{Pt}} + x_{\text{Co}} = 1$. As the total number of Pt–Co bonds and the total number of Co–Pt bonds should be identical, eq 1 must be satisfied. $R_{\text{Pt–Co}}$ and $R_{\text{Co–Pt}}$ are bond lengths, and $\sigma_{\text{Pt–Co}}^2$ and

$\sigma_{\text{Co–Pt}}^2$ are uncertainties of bond lengths after the fitting. As Pt–Co and Co–Pt bonds are identical, eqs 2 and 3 must be satisfied, too. The fitting results are listed in Table 5.

The two bimetallic catalysts have similar Pt–Co bond lengths. According to Vegard's law,⁴² they have similar compositions in the alloy phase; i.e., in the alloy phase both catalysts have a Co:Pt ratio of about 2, less than the bulk Co:Pt ratio, which is 3.31. Therefore, both catalysts have a Co core with a Pt–Co alloy shell. The existence of a Co core phase is consistent with the large average Co–Co coordination numbers from the EXAFS fitting results. Note that EXAFS is very insensitive to polydispersity. Also polydispersity and inhomogeneous distribution of the metals over the particles have only limited influence on the ability to distinguish between core shell particles and particles with random distribution of both metals.⁴³

The monometallic Pt–Pt bonds are negligible for both catalysts, indicating that for both catalysts, Pt atoms are almost atomically dispersed, which is consistent with the qualitative information obtained from Figure 3a. However, for Co–Co monometallic bonds, the Pt–Co/cSWNT-r has higher Co–Co average coordination number than Pt–Co/cSWNT-n. Further analysis can be carried out by taking the ratio between the average coordination numbers of Co–Co bonding and Co–Pt bonding. CN_{Co–Co}/CN_{Co–Pt} for Pt–Co/cSWNT-r is 3.86, larger than the atomic ratio between Co and Pt in the catalyst ($x_{\text{Co}}/x_{\text{Pt}} = 3.31$), indicating that in Pt–Co/cSWNT-r, the Co atoms prefer to bond with themselves rather than with Pt. Pt–Co/cSWNT-n, on the other hand, has a CN_{Co–Co}/CN_{Co–Pt} ratio of 2.57, indicating that in this catalyst Co atoms prefer to bond with Pt than with another Co.⁴⁰ These results suggest that Pt–Co/cSWNT-r has a larger Co core than Pt–Co/cSWNT-n. Consistent with this view, the TEM images in Figure 4 suggest that Pt–Co/cSWNT-r has larger particles than Pt–Co/cSWNT-n. Chemisorption results in Table 2 also show that Pt–Co/cSWNT-r has fewer active sites, probably due to the larger particle size.

The EXAFS analysis result shows how the SWNT support affects the catalyst structure. The introduction of defects and OCGs in the SWNT support does not affect the structure of the Pt monometallic catalysts significantly but has a large impact on the bimetallic catalysts. On the SWNT treated with HNO₃, Co in the bimetallic catalyst tends to bond with Pt rather than itself, leading to smaller particle size and more active sites. The different catalyst characteristics on SWNT supports with and without HNO₃ treatment is probably a result of the HNO₃ treatment introducing OCGs on the SWNT surface, so the hydrophilicity of the SWNT is changed. But having more active sites does not necessarily lead to higher activity. The APR activity test in Table 3 clearly shows that the change of support properties not only affects the catalyst structure (number of active sites) but also affects the catalytic reactivity (the activity per active site), due to the interaction of the support with the reactants.

3.4. Effect of Oxygen Containing Groups. The negative effect of oxygen containing groups (OCGs) on APR activity (TOF) over MWNT supported Pt catalysts has been discussed in our previous paper.¹³ From Table 3 it can be concluded that the support effect exists for SWNT supported catalysts, regardless of the TOF definition. Apparently, the OCGs have a more profound influence on the APR activity over SWNT supported monometallic catalysts than the activity over the bimetallic catalysts. To seek an explanation, in situ RGA measurements were conducted during the prereduction of the catalysts. The results in Figure 5 show that the reduction of Pt–Co/cSWNT-n

TABLE 5: EXAFS Fitting Results for Pt–Co Bimetallic Catalysts

catalyst	absorber	scatterer	CN ^a	dR (Å) ^b	R (Å) ^c
Pt–Co/cSWNT-r	Pt	Pt	N/A ^f	N/A ^f	N/A ^f
		Co	6.47 (1.45) ^d	−0.17 (0.01) ^d	2.60 ^e
	Co	Pt	1.94 ^e	0.11 ^e	2.60 ^e
		Co	7.49 (0.53) ^d	0.00 (0.00) ^d	2.50 ^e
Pt–Co/cSWNT-n	Pt	Pt	N/A ^{f,g}	N/A ^{f,g}	N/A ^{f,g}
		Co	7.26 (0.78) ^{d,g}	−0.19 (0.01) ^{d,g}	2.58 ^{e,g}
	Co	Pt	2.18 ^{e,g}	0.08 ^{e,g}	2.58 ^{e,g}
	Co	Co	5.60 (0.51) ^{d,g}	0.00 (0.00) ^{d,g}	2.50 ^{e,g}

^a First shell average coordination number of each absorber–scatterer pair. ^b Deviation from the interatomic distance in pure metal, which is 2.77 Å for Pt and 2.50 Å for Co. ^c Calculated bond length from dR. ^d Data from the first shell coordination number fitting; data in the brackets are uncertainties given by the IFEFFIT software. ^e These data are not directly from the fitting, thus uncertainty data are not included. ^f Pt–Pt bonds are not detectable within the error range of our experiments and fittings. ^g Data from ref 14.

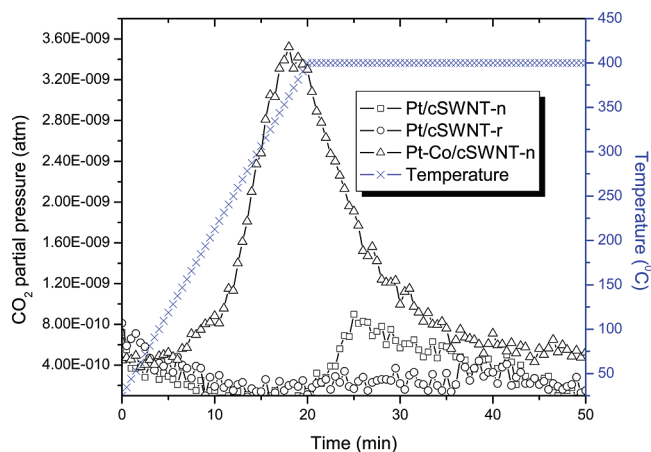


Figure 5. RGA results of the catalysts during prereduction.

releases a large amount of CO₂, which is probably from the decomposition of OCGs on the SWNT surface,⁴⁴ while the reduction of Pt/cSWNT-n releases much less CO₂, and CO₂ is released at a higher temperature. The two catalysts supported on cSWNT-r release negligible amount of CO₂ within the detection limit of the RGA (for reasons of clarity, only one curve is shown in Figure 5). The RGA results suggest that the bimetallic catalyst catalyzes the decomposition of OCGs from SWNT, while the Pt monometallic catalyst has poor efficiency in catalyzing the decomposition of OCGs, as reflected in the less intense CO₂ peak and higher temperature in the RGA results.

The difference in OCG decomposition can also be deduced from the IR spectra, shown in Figure 6. Both catalysts supported on cSWNT-n, after prereduction, retain the features of the OCGs, including the individual –OH bond at 3740 cm^{−1} and the hydrogen-bonded –OH bond at 3420 cm^{−1}. However, Pt/cSWNT-n has more intense peaks at both positions than Pt–Co/cSWNT-n. So the IR spectra verifies the RGA results that the Pt–Co bimetallic catalyst is more efficient in OCG removal during the prereduction procedure, leading to less OCG effect in APR reaction. There are still some OCGs left, as seen in the IR spectrum of Pt–Co/cSWNT-n, so the TOF of Pt–Co/cSWNT-n is still a little lower than Pt–Co/cSWNT-r, but the difference is not as profound as for the Pt monometallic catalysts with many OCGs left on the support.

4. Conclusion

Pt monometallic and Pt–Co bimetallic catalysts have been prepared on SWNT with and without HNO₃ treatment. The HNO₃ treatment introduced oxygen containing groups (OCGs), which affect both the structure and activity of the catalyst. The

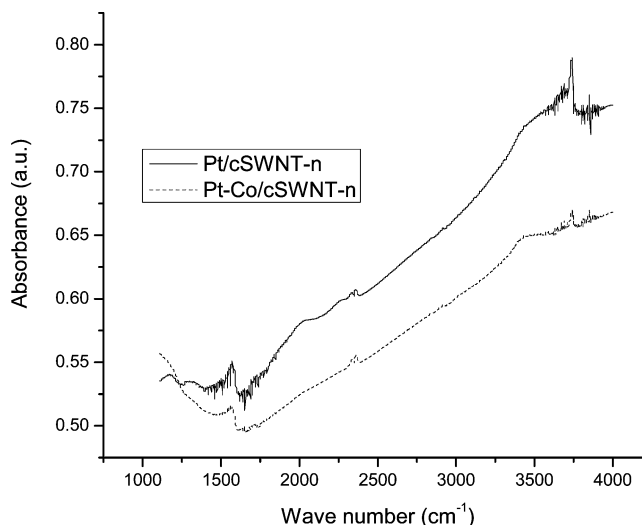


Figure 6. IR spectra of the catalysts after prereduction.

OCGs seem to have little effect on the structure of Pt monometallic catalysts, but for Pt–Co bimetallic catalysts, although both catalysts have core–shell structures with Co as the core and Pt–Co alloy as the shell, the introduction of OCGs alleviated the self-aggregation of Co thus decreases the size of the Co core in the core–shell structure, leading to smaller particle size and more active sites.

The OCGs also affect the APR activity, as suggested by our previous work on MWNT supported catalysts. The effect of OCGs on activity mainly comes from the competitive adsorption of the ethylene glycol and water on the catalyst surface in the APR reaction. The introduction of OCGs increases the hydrophilicity of the SWNT support and, therefore, the local concentration of water around the support. The decrease in the local concentration of ethylene glycol leads to lower activity in terms of TOF. The increase of active sites and the decrease of TOF affect activity in opposite directions, leading to similar catalyst mass time yields, but these observations give us an understanding and provide direction for future design of catalysts with higher dispersion and better activity.

Acknowledgment. We are grateful to the DOE, Office of Basic Energy Sciences, grant DE-FG02-05ER15732, and AFOSR MURI grant FA9550-08-0309 for financial support. Use of beamlines X18B and U7A, National Synchrotron Light Source, Brookhaven National Laboratory, was supported by the U.S. Department of Energy, Office of Science, Office of Basic Energy Sciences, under Contract No. DE-AC02-98CH10886. We also acknowledge Drs. Nebojsa Marinkovic and Chernoy Jaye for on-site technical help at NSLS.

References and Notes

- (1) Carrette, L.; Friedrich, K. A.; Stimming, U. *Chem. Phys. Chem.* **2000**, *1*, 162.
- (2) Li, Q. F.; He, R. H.; Jensen, J. O.; Bjerrum, N. J. *Chem. Mater.* **2003**, *15*, 4896.
- (3) Cheng, X.; Shi, Z.; Glass, N.; Zhang, L.; Zhang, J. J.; Song, D. T.; Liu, Z. S.; Wang, H. J.; Shen, J. *J. Power Sources* **2007**, *165*, 739.
- (4) Trimm, D. L.; Onsan, Z. I. *Catal. Rev.-Sci. Eng.* **2001**, *43*, 31.
- (5) Ghenciu, A. F. *Curr. Opin. Solid State Mater. Sci.* **2002**, *6*, 389.
- (6) Cortright, R. D.; Davda, R. R.; Dumesic, J. A. *Nature* **2002**, *418*, 964.
- (7) Shabaker, J. W.; Huber, G. W.; Davda, R. R.; Cortright, R. D.; Dumesic, J. A. *Catal. Lett.* **2003**, *88*, 1.
- (8) Shabaker, J. W.; Davda, R. R.; Huber, G. W.; Cortright, R. D.; Dumesic, J. A. *J. Catal.* **2003**, *215*, 344.
- (9) Davda, R. R.; Shabaker, J. W.; Huber, G. W.; Cortright, R. D.; Dumesic, J. A. *Appl. Catal. B-Environ.* **2005**, *56*, 171.
- (10) Huber, G. W.; Shabaker, J. W.; Evans, S. T.; Dumesic, J. A. *Appl. Catal. B-Environ.* **2006**, *62*, 226.
- (11) Huber, G. W.; Dumesic, J. A. *Catal. Today* **2006**, *111*, 119.
- (12) Trimm, D. L. *Appl. Catal. A-Gen.* **2005**, *296*, 1.
- (13) Wang, X. M.; Li, N.; Webb, J. A.; Pfefferle, L. D.; Haller, G. L. Submitted to *Appl. Catal. B-Environ.*
- (14) Wang, X. M.; Li, N.; Pfefferle, L. D.; Haller, G. L. *Catal. Today* **2009**, *146*, 160.
- (15) Li, W. Z.; Liang, C. H.; Zhou, W. J.; Qiu, J. S.; Zhou, Z. H.; Sun, G. Q.; Xin, Q. *J. Phys. Chem. B* **2003**, *107*, 6292.
- (16) Lordi, V.; Yao, N.; Wei, J. *Chem. Mater.* **2001**, *13*, 733.
- (17) Koningsberger, D. C.; Prins, R. *X-ray absorption: principles, applications, techniques of EXAFS, SEXAFS, and XANES*; Wiley: New York, 1988.
- (18) Newville, M. *J. Synchrotron Rad.* **2001**, *8*, 322.
- (19) Ravel, B.; Newville, M. *J. Synchrotron Rad.* **2005**, *12*, 537.
- (20) Alvarez, L.; Righi, A.; Guillard, T.; Rols, S.; Anglaret, E.; Laplaze, D.; Sauvajol, J. L. *Chem. Phys. Lett.* **2000**, *316*, 186.
- (21) Dresselhaus, M. S.; Dresselhaus, G.; Saito, R.; Jorio, A. *Phys. Rep.* **2005**, *409*, 47.
- (22) Murphy, H.; Papakonstantinou, P.; Okpalugo, T. I. T. *J. Vac. Sci. Technol. B* **2006**, *24*, 715.
- (23) Osswald, S.; Havel, M.; Gogotsi, Y. *J. Raman Spectrosc.* **2007**, *38*, 728.
- (24) Kuznetsova, A.; Popova, I.; Yates, J. T.; Bronikowski, M. J.; Huffman, C. B.; Liu, J.; Smalley, R. E.; Hwu, H. H.; Chen, J. G. *J. Am. Chem. Soc.* **2001**, *123*, 10699.
- (25) Oudenhuijzen, M. K.; Bitter, J. H.; Koningsberger, D. C. *J. Phys. Chem. B* **2001**, *105*, 4616.
- (26) Oudenhuijzen, M. K. Ph.D. Dissertation, Utrecht University, 2002.
- (27) Lu, S. L.; Lonergan, W. W.; Bosco, J. P.; Wang, S. R.; Zhu, Y. X.; Xie, Y. C.; Chen, J. G. *J. Catal.* **2008**, *259*, 260.
- (28) Lu, S. L.; Menning, C. A.; Zhu, Y. X.; Chen, J. G. *Chem. Phys. Chem.* **2009**, *10*, 1763.
- (29) Lu, S. L.; Qian, F.; Zhu, Y. X.; Xie, Y. C.; Chen, J. G. *Chin. J. Catal.* **2009**, *30*, 748.
- (30) Lu, S. L.; Lonergan, W. W.; Zhu, Y. X.; Xie, Y. C.; Chen, J. G. *G. Appl. Catal. B-Environ.* **2009**, *91*, 610.
- (31) Bazin, D.; Sayers, D.; Rehr, J. J.; Mottet, C. *J. Phys. Chem. B* **1997**, *101*, 5332.
- (32) Lytle, F. W.; Gregor, R. B.; Marques, E. C.; Sandstrom, D. R.; Via, G. H.; Sinfelt, J. H. *J. Catal.* **1985**, *95*, 546.
- (33) Yao, N. S.; Pinckney, C.; Lim, S. Y.; Pak, C.; Haller, G. L. *Microporous Mesoporous Mater.* **2001**, *44*, 377.
- (34) Guzzi, L.; Bazin, D.; Kovacs, I.; Borko, L.; Schay, Z.; Lynch, J.; Parent, P.; Lafon, C.; Stefler, G.; Koppany, Z.; Sajo, I. *Topics Catal.* **2002**, *20*, 129.
- (35) Park, J. I.; Kim, M. G.; Jun, Y. W.; Lee, J. S.; Lee, W. R.; Cheon, J. *J. Am. Chem. Soc.* **2004**, *126*, 9072.
- (36) Bazin, D.; Rehr, J. J. *J. Phys. Chem. B* **2003**, *107*, 12398.
- (37) Jacobs, G.; Chaney, J. A.; Patterson, P. M.; Das, T. K.; Maillot, J. C.; Davis, B. H. *J. Synchrotron Rad.* **2004**, *11*, 414.
- (38) Calvin, S.; Miller, M. M.; Goswami, R.; Cheng, S. F.; Mulvaney, S. P.; Whitman, L. J.; Harris, V. G. *J. Appl. Phys.* **2003**, *94*, 778.
- (39) Calvin, S.; Luo, S. X.; Caragianis-Broadbridge, C.; McGuinness, J. K.; Anderson, E.; Lehman, A.; Wee, K. H.; Morrison, S. A.; Kurihara, L. K. *Appl. Phys. Lett.* **2005**, *87*.
- (40) Frenkel, A. I. *Z. Kristallogr.* **2007**, *222*.
- (41) Knecht, M. R.; Weir, M. G.; Frenkel, A. I.; Crooks, R. M. *Chem. Mater.* **2008**, *20*, 1019.
- (42) Vegard, L. *Z. Phys.* **1921**, *5*, 17.
- (43) Moonen, J.; Slot, J.; Lefferts, L.; Bazin, D.; Dexpert, H. *Phys. B* **1995**, *208*, 689.
- (44) Sepulveda-Escribano, A.; Coloma, F.; Rodriguez-Reinoso, F. *Appl. Catal. A-Gen.* **1998**, *173*, 247.

JP102511K